Int. J. Electrochem. Sci., 16 **(2021)** Article ID: 210620, doi: 10.20964/2021.06.27

International Journal of
ELECTROCHEMICAL
SCIENCE
www.electrochemsci.org

Preparation of Micron-Sized Flower-Shaped SnO_2 Particles and Its Application as Anode Materials for Lithium Ion Batteries (LIBs)

Yuhong Chen

Department of Chemical and Environmental Engineering, Hebei Chemical & Pharmaceutical College, Shijiazhuang 050026, China
E-mail: chyh76@163.com

Received: 4 February 2021 / *Accepted:* 22 March 2021 / *Published:* 30 April 2021

For the first time, flower-shaped micron-sized tin dioxide (SnO_2) particles were prepared via an air calcination process using dibutyltin diacetate as the unique starting material. In this work, a proper amount of dibutyltin diacetate was calcined in air for 2 h under three calcination temperatures (300ºC, 500ºC and 700ºC), generating three samples (sample a, b and c, respectively.). It was indicated by the XRD and XPS analysis that SnO_2 with a relatively higher crystallinity was the main substance of above three prepared samples. Very interestingly, as displayed by the SEM images, spherical micron-sized particles, flower-shaped micron-sized particles and layered square rock-shaped particles were respectively observed in sample a, b and c. Most importantly, the initial discharge capacity (DC) of sample b at 100 mA g^{-1} was as high as 1067 mAh g^{-1}, and even after 20 cycles, the DC value of sample b was maintained to be 325 mAh g^{-1}, a value slightly lower than the theoretical specific capacity of graphite (372 mAh g^{-1}). Showing the fact that the direct calcination of dibutyltin diacetate was a feasible way to produce flower-shaped micron-sized SnO_2 particles, and drawing a conclusion that the calcination temperature and calcination time were all the important factors influencing the electrochemical performances of the resultant samples, were the main contributions of this preliminary work, which was very beneficial to the development of SnO_2-based anode materials of lithium ions batteries (LIBs) due to the very simple preparation procedure and lower preparation cost as well.

Keywords: dibutyltin diacetate; calcination; flower-shaped micron-sized SnO_2 particles; anode materials; lithium ion batteries (LIBs).

1. INTRODUCTION

Of late, the explosive growth of artificial intelligence (AI) products such as unmanned aerial vehicle (UAV) has tremendously stimulated the further development of lithium ion batteries (LIBs), which was mainly ascribed to the fact that LIBs was the most suitable kind of battery to power an AI

product due to its higher energy density and larger power density [1-3]. Therefore, how to improve the electrochemical performances of LIBs has become an urgent issue for all LIBs-related researchers [4, 5]. A LIB is generally composed of anode, cathode, electrolyte and separator, and etc., and every part of it was very closely related to the battery performance exhibited [6]. Although graphite, as a traditional anode material of LIBs, has been successfully commercialized for several decades, its evident drawbacks such as the lower theoretical capacity (372 mAh g^{-1}) [7] and the safety issue (The electrode potential of graphite is close to that of the metal lithium, thus, lithium dendrites will be produced at the surface of the graphite electrode especially when the LIBs were overcharged) immensely hindered the development of LIBs towards high power density and longer operation time [8]. Consequently, a large number of novel anode materials such as some novel kinds of carbon materials like graphene [9] and carbon nanotubes [10], some transition metal oxides like NiO[11] and Fe_2O_3[12], silicon-related material [13] and phosphorus based materials [14] have been urgently prepared in recent years in order to replace the present anode material of graphite as soon as possible. Unfortunately, thanks to the complicated preparation process and the relatively higher preparation cost, and the unsatisfied electrochemical performance as well, few of above developed materials were really applied as anode materials in the commercial LIBs, to our knowledge. Hence, seeking for novel anode materials of LIBs is still an urgent challenge for LIBs electrode material researcher. For all we know, among the transition metal oxides, tin dioxide (SnO_2) was regarded as one of the most feasible anode materials of LIBs mainly because of its rather higher theoretical capacity (1494 mAh g^{-1}) relative to graphite, environmental benignity and abundant reserves [15]. Therefore, especially recently, different strategies and various tin sources have been proposed to prepare SnO_2 particles with different morphologies desiring to produce SnO_2 particles with better electrochemical performance. For instance, SnO_2 nanotubes wrapped by porous carbon layers were successfully prepared by Lou's group [16] via a multistep method, in which MnO_x nanowires were employed as the templates and the tin source was $K_2SnO_3 \cdot 3H_2O$. Three-dimensional annealed SnO_2/graphene sheet foams were skillfully synthesized by Duan's group [17] employing an in situ self-assembly method where $SnCl_4 \cdot 5H_2O$ was employed as the starting material. Also, polydopamine-coated SnO_2 particles [18] were prepared using a template-based method where $Na_2SnO_3 \cdot 3H_2O$ was utilized as the tin source and five steps were involved in the whole preparation process. Except for above preparation methods, the process of ball milling was also employed to prepare ternary SnO_2-M-graphite composites (M = Fe, Mn, Co) where pristine SnO_2 and transition metal and graphite powders were utilized as the starting materials [19]. Of late, a laser-assisted pyrolysis process was developed by Srinivasan's group [20] for preparing N-doped SnO_2 nanoparticles where $SnCl_4 \cdot 5H_2O$ was utilized as the tin source. Nevertheless, as far as we know, till present, no paper reporting the synthesis of micron-sized SnO_2 particles through an air calcination method employing dibutyltin diacetate as the starting material was published.

To increase the electrical conductivities of SnO_2 particles, various kinds of carbon materials have been deliberately composited with SnO_2 particles to yield carbon-based SnO_2 particles. For instance, a skeleton-structured SnO_2/graphene composite was prepared via a spray-drying-induced assembly method by Li's team [21] where $SnCl_4 \cdot 5H_2O$ was the starting material. Very recently, a large number of materials consisting of carbon and SnO_2 particles, such as phosphorized SnO_2/graphene heterostructure based materials [22], multi-wall Sn/SnO_2@carbon hollow nanofibers [23], a composite

having a three-dimensional porous SnO_2@NC framework [24], and etc., [25] have been successfully prepared with an intention to further ameliorate the electrochemical performance of SnO_2. In 2020, SnO_2 nanoflowers decorated on N-doped carbon nanofibers [26] were fabricated through the hydrothermal growth of SnO_2 nanoflowers on the surface of carbon fibers, in which $SnCl_2 \cdot 2H_2O$ was the source of tin and the as-synthesized SnO_2 sample was assembled by numerous agglomerated nanosheets, rather than showing a layered structure. In a nutshell, being composited with carbon materials and preparing SnO_2 particles with special morphologies were the main two ways for promoting the electrochemical performance of SnO_2 particles. To our knowledge, no report describing the synthesis of a composite consisting of carbon materials and SnO_2 particles via an air calcination method employing dibutyltin diacetate as the starting material was issued thus far, and the preparation of flower-shaped micron-sized SnO_2 particles was also rarely reported based on our detailed literature survey.

Of late, carbon spheres (CSs), as one main kind of carbon materials, have received ever-growing research interest especially in the research field of electrochemistry mainly thanks to their higher electrical conductivities and lower preparation costs. Not only can CSs be used as a carrier to support an electrocatalyst, but also can CSs be employed as dopants of a composite so as to greatly enhance the electrical conductivity of the as-synthesized composite. Therefore, many strategies have been proposed to prepare CSs. For example, as early as in 2004, CSs with a diameter sizing from 200 nm to 1500 nm were prepared by Li's group [27] using a hydrothermal method where the as-prepared CSs were employed a carrier of silver nanoparticles. In 2014, porous carbon spheres were synthesized by Gogotsi's team [28] through a chemical reaction using liquid ammonia and resorcinol formaldehyde resin as the starting materials. An alginic acid-present hydrothermal carbonization method was also developed by Fan's group [29] to prepare porous hollow carbon spheres. Very recently, a pressure-assisted process employing glucose as the carbon source was designed by Zhang's group [30] to fabricate monodisperse hydrothermal carbon spheres. Meanwhile, CSs have been successfully doped into the metal-based composites so as to ameliorate the electrochemical performances of the composites studied. For instance, N-doped carbon hollow spheres [31] were skillfully doped into MoN forming a MoN @ N-doped carbon hollow sphere in which glucose was the carbon source for preparing N-doped carbon hollow spheres. In short, the hydrothermal process employing glucose as the starting material was the most widely used method to prepare CSs according to our literature research. For all we know, no work, describing the preparation of CSs via an air calcination method using the organometallic compound of dibutyltin diacetate as the raw material, was reported so far, though, as mentioned above, many approaches have been urgently developed to prepare CSs.

In this work, a proper amount of dibutyltin diacetate was directly calcined in air to generate the final samples. The samples calcined at 300ºC, 500 ºC and 700 ºC were, respectively, nominated as sample a, b and c. As indicated by XRD and XPS analysis, besides carbon material, SnO_2 was the main component of all prepared samples. As revealed by the SEM images, for sample b, except for the prepared CSs, flower-shaped micron-sized particles were distinctly exhibited. Most importantly, the DC value delivered by sample b at 100 mA g^{-1} even after 20 cycles was still maintained to be about 325 mAh g^{-1}, delivering the best electrochemical performance among the as-prepared three samples. In this work, a composite consisting of carbon spheres and flower-shaped SnO_2 particles was facilely

prepared by using a one-step method of calcination process, which was the main contribution of this work, being very beneficial to the booming of SnO_2 based anode materials of LIBs owing to its rather simple preparation process and relatively lower preparation cost.

2. EXPERIMENTAL DETAILS

2.1 Reagents and materials

The analytical chemical reagent of dibutyltin diacetate was purchased from Tianjin Reagent Company (China). All the materials used in the battery measurement such as the electrolyte of 1 M $LiPF_6$, separator, metallic lithium foil, acetylene black and PVDF (polyvinylidene fluoride) were bought from Tianjin Lianghuo S&T Developing Co. Ltd (China). The commercial current collectors of copper foils were provided by Hebei LingDian New Energy Technology Co., Ltd (Hebei Tangshan, China).

2.2 Fabrication of flower-shaped micron-sized SnO_2 particles

The preparation of flower-shaped micron-sized SnO_2 particles was accomplished through a very simple calcination method. 30 g of dibutyltin diacetate was placed in a crucible which was directly calcined in air atmosphere at 300ºC for 2 h in a muffle furnace. After cooling down to the room temperature, the resultant powders were thoroughly ground in an agate mortar at least for 20 min to produce the final samples. The as-prepared samples calcined at 300ºC, 500ºC and 700ºC were, respectively, nominated as sample a, b and c. And the samples calcined at 500ºC for 4 h and 6 h were, respectively, labeled as sample b_1 and b_2.

2.3 Characterization

X-ray diffraction (XRD) measurement was carried out on a XRD diffractometer (Bruker AXS, D8 ADVANCE, Germany) through which the crystal structure as well as the substance kinds of all prepared samples can be determined definitely. The surface morphologies of all resultant samples were viewed using scanning electron microscopy (HITACHI, SEM S-570). The elemental compositions of all synthesized samples were examined using energy dispersive spectrometer (EDS, INCA Energy 350, England). The functional groups existing in the as-synthesized samples were analyzed by using Fourier transform infrared spectrometry (FTIR, Hitachi FTIR-8900 spectrometer, Japan). And the chemical valences of all the elements existing in the prepared samples were detected by using X-ray photoelectron spectroscopy (XPS, Kratos Analytical spectrometer, Al Kα radiation) with an intention to further confirm the kinds of substances synthesized.

2.4 Preparation of as-prepared sample based electrode

The preparation of the as-prepared sample based anode of LIBs has been well described in the previous work [32]. In brief, a mixture containing sample a, acetylene black (AB) and polyvinylidene fluoride (PVDF) (the mass ratio of sample a, AB and PVDF was 8:1:1) was prepared firstly. And then, a proper amount of N-methylpyrrolidone (NMP) was added into above resultant mixture to generate a slurry-like cream after a vigorous stirring. Subsequently, the resultant creams were carefully painted on the surface of a copper foil current collector. Soon afterwards, the resulting sample a-coated Cu foils were heated in a vacuum oven at 120 ºC for 6 h in order to thoroughly expel all the volatile substances such as the solvents remained. The loading amount of sample a on each copper foil was about 1.5 mg cm^{-2}. The electrode prepared using sample a, b and c were, respectively, named as electrode a, b and c. The half-cell that was assembled in a glove box fully filled with N_2 (ZKX, Nanjing NanDa Instrument Plant, China) was employed to study the battery performance of the as-prepared samples. Except for a pure lithium foil and an above prepared electrode, the assembled half-cell also contained a separator of Celgard 2400 and an electrolyte of 1 M $LiPF_6$. Meanwhile, the organic solvent for dissolving $LiPF_6$ was a mixed solvent which was chiefly made up of dimethyl carbonate (DMC), ethylene carbonate (EC), vinylene carbonate (VC) and ethyl methyl carbonate (EMC). In the half-cell, the pure lithium foil was used as both negative electrode and the reference electrode. That is to say, the potential values appearing in this work were all relative to the electrode potential of the pure lithium foil used. The galvanostatic charge/discharge tests were conducted at room temperature on a battery tester (CT-3008W-5V20mA-S4, Shenzhen Neware Electronics Co., Ltd. China). The potential window was ranged from 0.01 V to 3 V in the charge/discharge measurement, and the current density of 100 mA g^{-1} was employed in the cycling measurements.

Cyclic voltammetry (CV) and electrochemical impedance spectroscopy (EIS) of the assembled half-cells were all carried out on an apparatus of CHI 660B (Shanghai Chenhua Apparatus, China) to further investigate the charge-discharge mechanism of lithium ions in the as-synthesized samples. The frequency range and alternating current (AC) amplitude of the EIS measurement were, respectively, from 1 Hz to 100 kHz and 5 mV. Additionally, all the EIS measurements were conducted at the open circuit potentials of the assembled half-cells.

3. RESULTS AND DISCUSSION

3.1 Characterizations of all prepared samples

The photos for all involved samples are given in Fig.1. The starting material of dibutyltin diacetate was a colorless transparent liquid. And the samples prepared under the calcination temperature of 300ºC, 500 ºC and 700 ºC, respectively, delivered a reddish brown color, brown color and grayish white color. XRD patterns for all prepared samples are shown in Fig.2a. For sample a (pattern a), no evident sharp diffraction peaks were exhibited suggesting that no substances with higher crystallinity were fabricated in sample a. Careful observation indicated that a weak and broad

diffraction peak was exhibited in the Bragg angle range from 20º to 30º in pattern a, demonstrating the presence of amorphous carbon in sample a, which should be attributed to the incomplete combustion of dibutyltin diacetate in the calcination process.

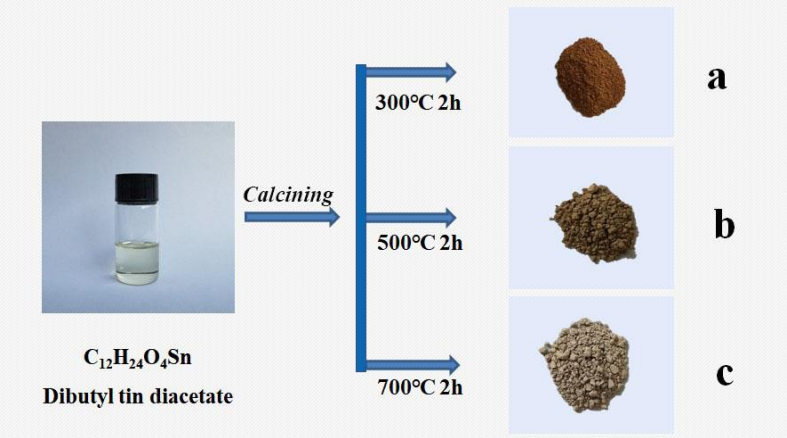

Figure 1. Photos for the starting material of dibutyltin diacetate and the as-prepared samples. The colorless transparent liquid in the vial was dibutyltin diacetate. The powder with reddish brown color, brown color and grayish white color corresponded to the powder of sample a, b and c, respectively.

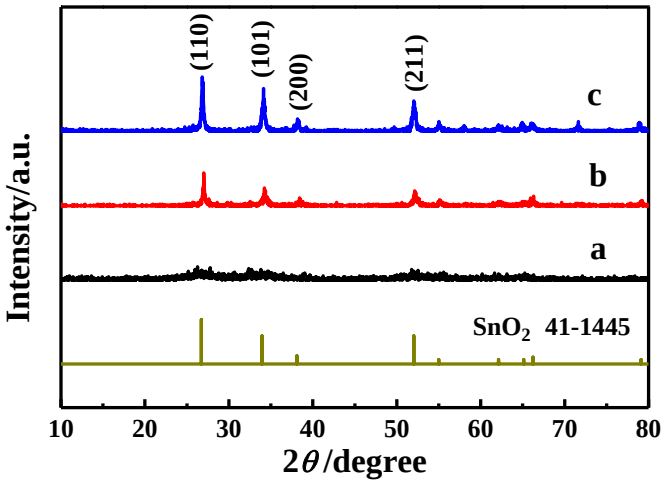

Figure 2a. XRD patterns for all synthesized samples. Pattern a, b and c corresponded to sample a, b and c.

While for sample b and c, through comparing with the standard XRD patterns of SnO_2 (JCPDS No. 41-1445), four obvious diffraction peaks assigned to SnO_2 were clearly exhibited, indicating the successful preparation of SnO_2 in sample b and c. That is, the diffraction peaks positioned at 26.9º, 34.1º, 38.2º and 52.0º were, respectively, indexed to the reflection plane (110), (101), (200) and (211) of the SnO_2, implying that SnO_2 particles [21] with relatively higher crystallinity were prepared in both

sample b and c. Additionally, the intensities of the diffraction peaks of sample c were remarkably higher than that for sample b, indicating that the calcination temperature was a vital factor which could greatly affect the crystallinity of the final calcination products.

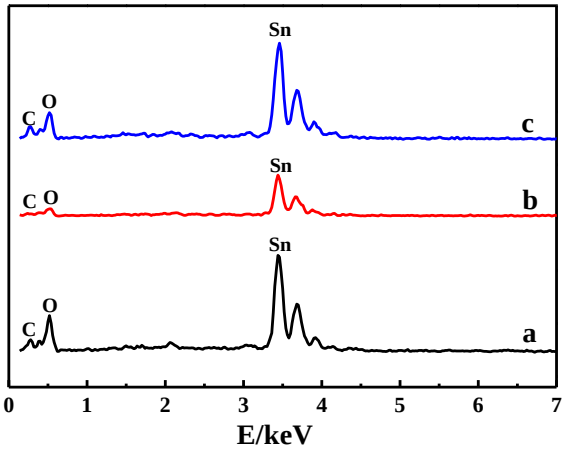

Figure 2b. EDS patterns for all prepared samples. Pattern a, b and c corresponded to sample a, b and c.

The EDS patterns of above three synthesized samples are presented in Fig.2b where the peaks ascribed to C, O and Sn elements were all clearly exhibited, indicating that carbon material and Sn-based oxides were the main substances of the resultant samples. The atomic contents of C in sample a, b and c were approximately detected to be 15.1%, 16.5% and 19.1%, respectively. Generally, the presence of a proper amount of carbon material, due to its higher electrical conductivity, in a metal oxide based anode material was very advantageous to the electrochemical performance improvement of an anode material [33]. The atomic contents of Sn and O elements in sample a, b and c were roughly detected to be 11.4% and 73.5%, 16.1% and 67.4%, 12.6% and 68.3%, respectively. Apparently, the atomic content ratio of O to Sn for all prepared samples was greater than two, indicating that the carbon material existing in all prepared samples was a composite carbon material which was decorated by many oxygen-containing functional groups. Also, sample b had the largest atomic content of Sn element among above three prepared samples, suggesting that more amounts of SnO_2 were prepared in sample b, which was very beneficial to the charge capacity promotion since tin dioxide itself was a lithium storage material [34].

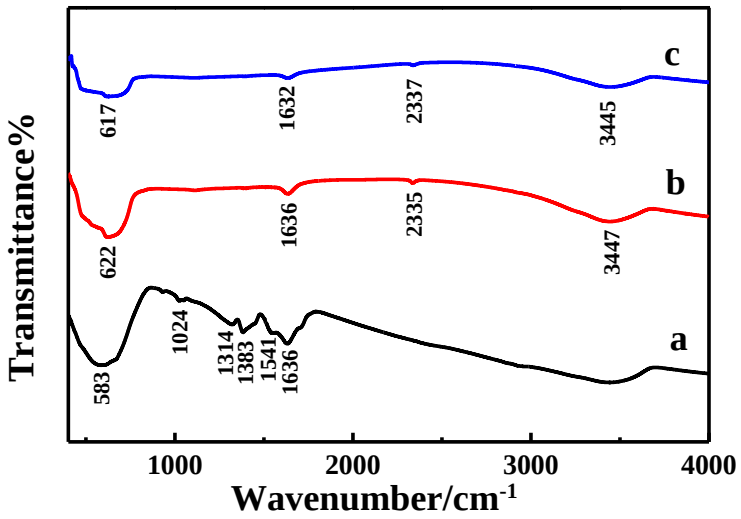

Figure 2c. FTIR spectrum of all as-prepared samples. Curve a, b and c corresponded to sample a, b and c.

FTIR spectra of all as-synthesized samples are plotted in Fig.2c where several evident adsorption bands were displayed in the longer wave number region, authenticating the presence of organic functional groups in all prepared materials. The broad adsorption band positioned at about 3445 cm^{-1} can be indexed to O-H bending vibrations, showing the presence of hydroxyl groups in the all synthesized samples [35]. Also, for all prepared samples, a broad adsorption peak centered at 583, 622 and 617 cm^{-1} was, respectively, observed in the FTIR spectrum for sample a, b and c, which was generally attributed to the presence of Sn-O chemical bond in all resultant samples [21]. Also, the shape of the adsorption peaks appearing both at 622 cm^{-1} (sample b) and 617 cm^{-1} (sample c) was very similar to that of the pure SnO_2 [36], implying that the purity of SnO_2 prepared in both sample b and c was higher than that of SnO_2 synthesized in sample a. In addition, in the case of sample a, several adsorption peaks appeared in the wave number region ranging from 1000 cm^{-1} to 2000 cm^{-1}, implying that more organic functional groups were prepared in sample a. Generally, the adsorption bands centered at 1541 and 1636 cm^{-1} were stemmed from the stretching vibrations of carboxyl groups [37]. While for sample b and c, only four adsorption peaks were presented in the whole wave number range which substantially indicated that more amounts of carbon-containing substances have been completely burned out when the calcination temperature was higher than 300ºC. The adsorption band positioned at 1636 cm^{-1} for sample b and that centered at 1632 cm^{-1} for sample c should be all originated from the water bending mode based on the previous work [38]. FTIR spectra shown in Fig.2c at least indicated that, compared to sample a, less amounts of carbon-containing materials were prepared in sample b and c, being consistent with the results of XRD analysis (Fig.2a).

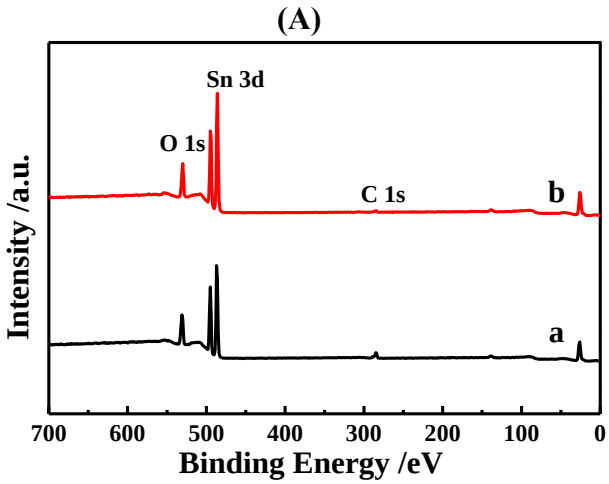
(A)
Sn 3d
O 1s
C 1s
b
a
Intensity /a.u.
700
600
500
400
300
200
100
0
Binding Energy /eV

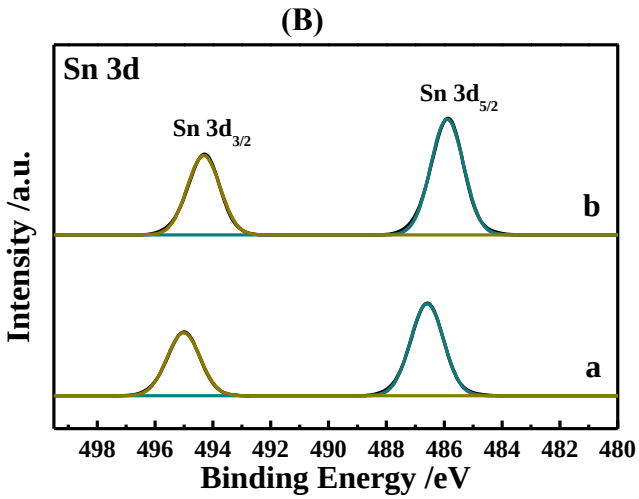
(B)
Sn 3d
Sn 3d3/2
Sn 3d5/2
b
a
Intensity /a.u.
498
496
494
492
490
488
486
484
482
480
Binding Energy /eV

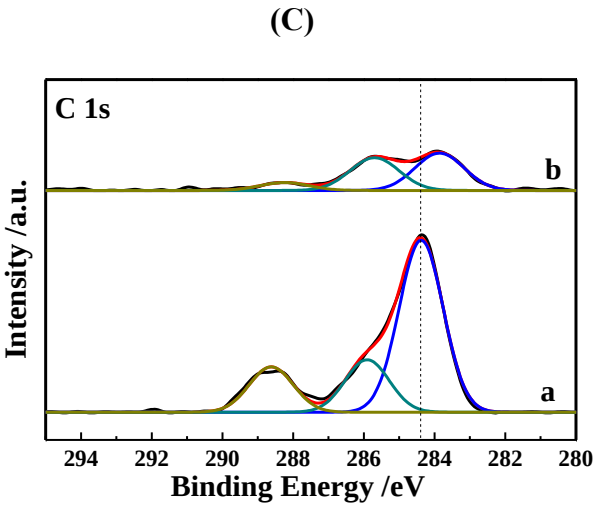
(C)
C 1s
b
a
Intensity /a.u.
294
292
290
288
286
284
282
280
Binding Energy /eV

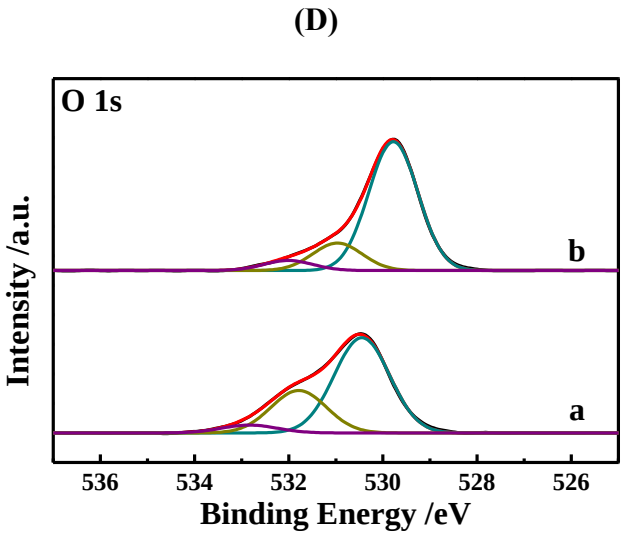

Figure 3. XPS spectrum for sample a and b, in which pattern a and b corresponded to sample a and b, respectively. **(A)** Wide scan XPS survey spectra. **(B)** High resolution Sn 3d XPS spectra. **(C)** High resolution C 1s XPS spectra. **(D)** High resolution O 1s XPS spectra.

XPS patterns for sample a and b are given in the serial figures of Fig.3. It should be noted that the shape of XRD pattern and FTIR curve for sample b, as shown in Fig.2a and Fig 2c, was very similar to that for sample c, thus, XPS patterns for sample c were not recorded in this work. In figure A of Fig.3, the peaks assigned to O, Sn and C elements were all exactly displayed tallying well with the EDS results (Fig.2b.). Also, no peaks indexed to other elements were exhibited, suggesting that no other impurities were formed in the synthesized samples. Consequently, it could be deduced indirectly that tin oxides and carbon materials were the principal substances of above three synthesized samples. As shown in figure B of Fig.3, for sample b, the signal peaks at binding energies (BE) of 494.3 eV and 485.8 eV were well assigned to Sn $3d_{3/2}$ and Sn $3d_{5/2}$, respectively, according to the previously reported XPS pattern of the pure SnO_2 [36]. Meanwhile, the BE values of Sn $3d_{3/2}$ and Sn $3d_{5/2}$ for sample b were all negatively shifted for 0.5 eV as compared to the case of the pure SnO_2 (pure SnO_2, Sn $3d_{3/2}$ (494.8 eV) and Sn $3d_{5/2}$ (486.3 eV)), which was mostly attributed to the presence of carbon materials in sample b [36]. While for sample a, the two signal peaks at BE values of 486.5 eV and 495.0 eV can also be assigned to Sn $3d_{5/2}$ and Sn $3d_{3/2}$, respectively. The slight shifting of the peak BE value was generally resulted from the interaction between SnO_2 and carbon materials or due to the variation of the interface region heterojunction of between SnO_2 and the as-prepared carbon materials [21]. The high resolution XPS spectra of C1s for sample a and b are illustrated in figure C of Fig.3. In the case of sample a, the BE peaks positioned at 284.3, 285.9 and 288.6 eV were, respectively, attributable to the presence of sp^2-C, C-OH and O=C-OH groups, being indicative of the existence of carboxyl and hydroxyl groups in all synthesized samples, being in line with the result of the FTIR spectra (Fig.2c) [39,40]. While for sample b, the intensities of the BE peaks assigned to C1s, as compared to the case of sample a, were all greatly reduced suggesting that more amount of carbon materials in sample b were consumed when the calcination temperature was increased to be 500ºC. The BE peaks assigned to sp^2-

C group (at 283.9 eV) and C-OH group (at 285.6 eV) were clearly observed in sample b strongly indicating that carbon materials with carboxyl groups were still remained in sample b, being in accordance with the analysis of the FTIR spectra (Fig.2c). In the high resolution XPS spectrum of O1s for sample a and b (figure D of Fig.3), three fitted peaks were displayed distinctly being indicative of the presence of three kinds of oxygen in the prepared samples. For sample b, the BE peak positioned at 530.4 eV and that at 531.0 eV were, respectively, indexed to the Sn-O bond of SnO_2 and C=O bond of carbonyl or carboxyl group [40, 41]. The smallest peak for sample b located at 532.0 eV should be assigned to C-O-C or C-OH group [17, 41]. While for sample a, compared to that of sample b, all the peak positions were positively shifted for about 0.8 eV which was mainly due to the variation of the chemical compositions. XPS spectra shown in Fig.3 further confirmed that SnO_2 was the main tin-containing substance of all synthesized samples, and carbon materials containing a large number of hydroxyl and carboxyl groups were produced in all resultant samples.

3.2 SEM characterization

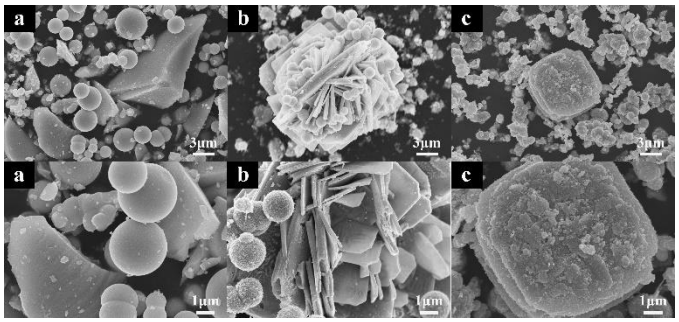

Figure 4. SEM images with scales of both 3 μm and 1μm for as-synthesized samples. Image a, b and c corresponded to sample a, b and c.

SEM images with various scales of the surface morphologies for all prepared samples are presented in Fig.4. A large number of spherical particles with different sizes and several huge irregular particles as well were clearly displayed in sample a (image a), and as indicated by image a with a scale of 1 μm, all the resultant spherical particles had a smooth surface and most of their particle sizes were larger than 1μm. For sample b (image b with a scale of 3μm), besides some small spherical particles, a huge aggregate constructed by many flaky particles was presented distinctly, forming a flower-shaped morphology. Only O and C elements were detected in the fixed EDS patterns of those small spherical particles of sample b, which strongly demonstrated that those small spherical particles appearing in sample b were carbon spheres. As seen by the image b with a scale of 1μm, a great many of protuberances were seen on the surface of these synthesized small particles generating a spiny and uneven surface, and all the resultant flaky particles exhibited a rectangle shape and the thickness of each flaky particle was close to 210 nm. Interestingly, in the case of sample c (image c), no small spherical particles were displayed any more, revealing the diminishing of carbon spheres with increasing the calcination temperature. Also, the flaky particles appearing in sample b could not be observed any longer in sample c, instead, a huge particle with a layered square rock morphology,

which looked like a Chinese layered moon cake, was clearly presented. Therefore, it was reasonable to believe that the calcination temperature played a vital role in influencing the morphology of the final samples. The difference in morphology of the prepared samples, generally, indicated that the components of the synthesized samples were different from each other, which was well consistent with the XRD (Fig.2a) and XPS (Fig.3) results.

3.3. Electrochemical performance of the prepared samples as LIBs anode materials

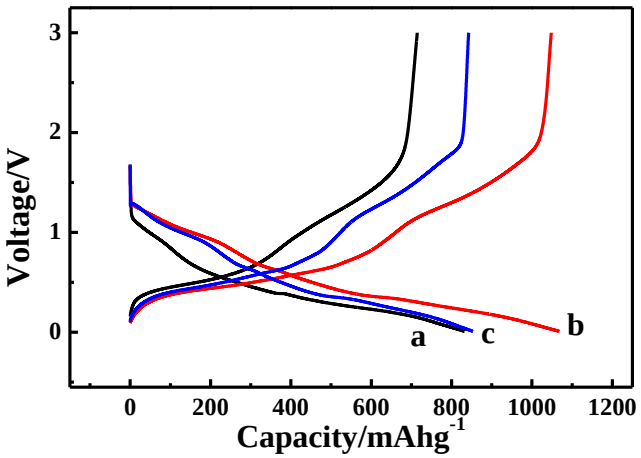

Figure 5a. The initial charge-discharge patterns measured at 100 mA g^{-1} for all prepared samples. Curve a, b and c corresponded to sample a, b and c.

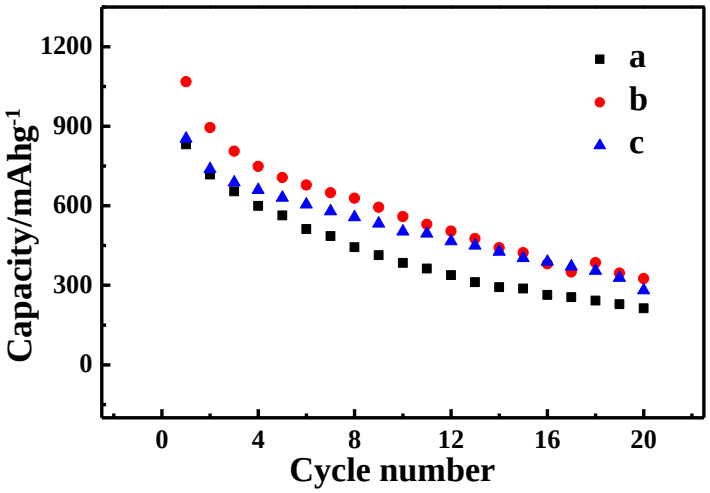

Figure 5b. The cycling performances of all prepared samples at 100 mA g^{-1}. Curve a, b and c corresponded to sample a, b and c.

The initial charge-discharge profiles of all prepared samples at 100 mA g^{-1} are depicted in Fig.5a in which the potential range was from 0.01 V to 3 V. In the charging process, an oblique line followed by an evident step was observed in the potential limit from 0.1V to 1.9 V, and in the

discharging process, a sloped line followed by a weak step was exhibited in the potential region ranging from 1.26 V to 0.1 V. The shape of the charge-discharge curves shown in Fig.5a was very similar to that of SnO_2 based LIBs anode materials [23, 42], further testifying that the as-prepared SnO_2 was the main lithium storage material of all synthesized samples. The initial discharge capacities of sample a, b and c, based on the curves shown in Fig 5a, were estimated to be 831, 1067 and 853 mAh g^{-1}, respectively. The cycling performances of all prepared samples at 100 mA g^{-1} are also given in Fig.5b in which the discharge capacity (DC) values of all the resultant samples delivered an evident decreasing trend in the whole testing period. After 20 cycles, the DC values for sample a, b and c decreased from 831 to 215 mAh g^{-1}, from 1067 to 328 mAh g^{-1} and from 853 to 276 mAh g^{-1}, respectively, corresponding to the capacity retention values of 25.8%, 30.7% and 32.3%. It should be emphasized that the DC value of 328 mAh g^{-1} for sample b was dramatically higher than that of the previously reported value of pure SnO_2 (201.8 mAh g^{-1} after 25 cycles at 200 mA g^{-1}) [17]. Therefore, sample b exhibited a better battery performance in terms of the initial DC value and the cycling performance.

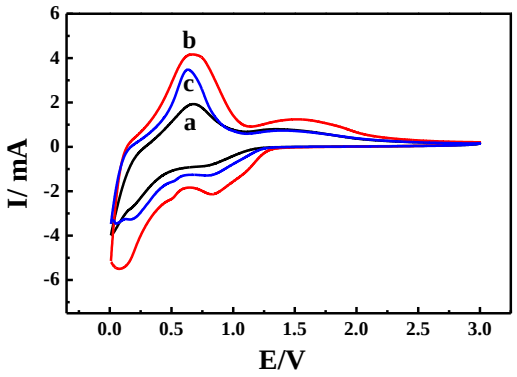

Figure 6a. Cyclic voltammetry (CV) curves for the as-synthesized samples at 1 mV s^{-1}. Curve a, b and c corresponded to sample a, b and c.

The cyclic voltammetry (CV) curves recorded at 1 mV s^{-1} of all produced samples are plotted in Fig.6a. For all the samples, two electro-oxidization peaks, respectively, positioned at 0.6 V and 1.48 V, were exhibited in the positive potential scanning, suggesting that two deintercalation processes of lithium ion were contained in the charging process. While in the negative potential scanning, besides the large reduction peak appearing at about 0.01V, only one small and weak electro-reduction peak centered at about 0.78V was displayed in the CV curve of sample a. And for sample b and c, except for the large electro-reduction peak at around 0.01V, two electro-reduction peaks were found to be successively at 0.81V and 0.18V, respectively. Generally, the electro-oxidation peak at 0.6V was attributed to the dealloying of Li_xSn to Sn, namely, $Li_xSn\text{-}xe^- \rightarrow Sn+xLi^+$, and the electrooxidation peak at 1.48V was assigned to the reversion of Sn/Li_2O to produce SnO_2, namely, $Sn+ 2Li_2O\text{-}4e^- \rightarrow SnO_2 + 4Li^+$ based on the previous work concerning SnO_2 [18]. Correspondingly, the electroreduction peak at 0.81 V should be originated from the electrochemical reaction of SnO_2, namely, $SnO_2 + 4Li^+ + 4e^- \rightarrow Sn+ 2Li_2O$, and electroreduction peak appearing at 0.18V should correspond to the

electrochemical reaction of $Sn+xLi^{+}+xe^{-}\rightarrow Li_xSn$. The CV peaks appearing at 0.01V were generally thought to be stemmed from the reaction of $LiC_6\text{-}6e^{-}\rightarrow C+ 6Li^{+}$(in the charging process) and $C+ 6Li^{+} +6e^{-}\rightarrow LiC_6$ (in the discharging process)[23]. The shape of the CV curves exhibited in Fig.6a was very analogous to that of pure SnO_2, again confirming that SnO_2 was the principle lithium storage material of all prepared samples. Evidently, the largest CV peak area was displayed by sample b among all studied samples, implying that the largest amounts of lithium ions were transferred in sample b, according well with the results shown in Fig.5a and 5b.

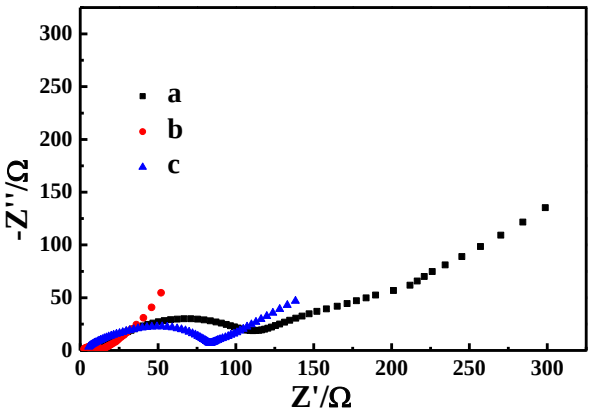

Figure 6b. Nyquist plots of all as-synthesized samples. Plot a, b and c corresponded to sample a, b and c.

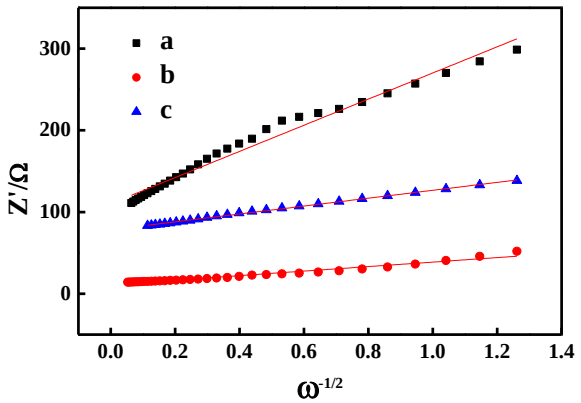

Figure 6c. Curves showing the relationship between Z' and $\omega^{-1/2}$. Curve a, b and c corresponded to sample a, b and c.

Nyquist plot as one main kind of the curves in EIS has been applied as a convenient and practical tool to study the electrochemical performance of a LIB. The Nyquist plots of all the assembled half-cells are shown in Fig.6b. Evidently, the Nyquist plots of all prepared samples were constituted by a semicircle appearing in the higher frequency limit and a sloped line emerging in the lower frequency range, showing a routine Nyquist plot shape of a half-cell lithium ion battery [43, 44].

According to the previous work [45], the diameter of the semicircle existing in the higher frequency region was approximately equal to the charge transfer resistance value (R_{ct}). And the smaller the R_{ct} value is, the faster the kinetics of lithium ion is delivered [45]. The R_{ct} values were estimated to be 110, 15 and 85 Ω for sample a, b and c, respectively. Hence, the fastest kinetics of lithium ion was exhibited by sample b, agreeing well with the fact that sample b delivered the largest discharge capacity value among all resultant samples.

The lithium ion diffusion coefficients of D_{Li}^+ for all prepared samples were also evaluated employing the data acquired from Fig.6b, and the curves showing the relationship between Z_{re} and $\omega^{-1/2}$ were plotted in Fig. 6c based on the following equation (1) [46].

$$Z_{re}=R_s+R_{ct}+\sigma\omega^{-1/2} \quad (1)$$

In above equation, Z_{re}, the real part of the impedance, was the value of Z' presented in Fig.6b. R_s was the solution resistance of an electrochemical reaction, and for a half-cell, R_s was generally described as the total resistance of the half-cell, which roughly corresponded to the first intercept value at the Z' axis in the Nyquist plot. As described previously, R_{ct} was the charge transfer resistance, whose value approximately amounted to the diameter of the semicircle appearing in the higher frequency region. ω, nominated as angular frequency, had a relationship with frequency, i.e., $\omega=2\pi f$. Therefore, the slope of the line showing the relationship of between Z_{re} and $\omega^{-1/2}$ was the value of σ. And then, the value of σ was put in equation (2) [47] to calculate the final value of D_{Li}^+

$$D_{Li^+} = \frac{(RT)^2}{2(An^2F^2C_{Li^+}\sigma)^2} \quad (2)$$

In above equation, the parameters of T, R and F had their traditional scientific meanings. A was the surface area of an electrode. And n and C_{Li}+, respectively, corresponded to the number of electrons of an electrochemical reaction and the Li^+ concentration of an electrode material. As discussed above, all prepared samples in this work were novel substances. Hence, the values of C_{Li}+ of all synthesized samples were unknown to us. For simplicity, besides the value of σ, the values of all other parameters in equation (2) were assumed to be identical in each sample. That is, the smaller value of σ should correspond to a larger value of D_{Li}^+. It was clear, as shown in Fig.6c, that the lowest value of σ was exhibited by sample b, signifying that sample b had the largest value of D_{Li}+ among all produced samples.

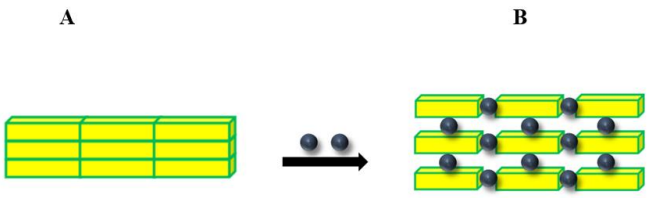

Figure 7. The diagrammatic sketch of the spatial configuration for sample b. The yellow cuboid with green edge and the black spherical particles represented the flaky SnO_2 particle and the carbon sphere, respectively. Part A corresponded to the case in the absence of carbon spheres in which flaky SnO_2 particles were closely piled up forming a huge wall-shaped agglomeration. Part B corresponded to the case in the presence of carbon spheres where some carbon spheres were inserted in between the resultant flaky SnO_2 particles forming a three dimensional spatial structure.

Why did sample b deliver the best battery performance among prepared samples? As shown in Fig.4, sample b had a flower-shaped morphology, generating a rather peculiar configuration. A diagrammatic sketch for describing this particular configuration was presented in Fig.7. That is, in the absence of small spherical particles (carbon spheres), these flaky SnO_2 particles were tightly piled up forming a wall-shaped deposit (part A of Fig.7.). Therefore, a plenty of boundaries were created at the interfaces of between the resultant flaky SnO_2 particles. While in the presence of carbon spheres, as shown by part B of Fig.7, the interfaces of between the prepared SnO_2 particles were fully filled with the as-prepared carbon spheres producing a three dimensional structure. In this case, the interface of between two SnO_2 particles was substituted by a novel interface of between SnO_2 particles and carbon spheres, leading to a significantly decreased interface resistance (Usually, the interface resistance value of between two SnO_2 particles was obviously larger than that of between one SnO_2 particle and one carbon sphere, due to the higher electrical conductivity of carbon materials as compared to metal oxides), which has been well corroborated by Nyquist plots shown in Fig.6b. That is to say, many prepared carbon spheres were inserted in between flaky SnO_2 particles, acting as conducting wires to connect all SnO_2 particles closely, forming a conducting wires-constructed three dimensional network. As reported previously [48], carbon spheres could be regarded as cushions in the metal oxides based anode materials of LIBs, which could greatly accommodate the remarkable volume variation of SnO_2 particles in the cycling process, preventing anode materials from cracking in some degree. Also, as compared to the case of part A in Fig.7, each SnO_2 particle was wetted by more electrolytes which would lead to an increase in the contacting area of between SnO_2 particle and the electrolyte, which was very beneficial to greatly lower the over-potential of the phase interfaces. Summarily, the markedly increased electrical conductivity arising from the presence of carbon spheres, the special spatial structure of 3D configuration, the buffering effect arising from the prepared carbon spheres and the greatly lowered phase interface over-potential were the main reasons for sample b to exhibit the best electrochemical performance among above three synthesized samples.

In this work, the influence of the calcination temperature on the electrochemical properties of the resultant samples prepared using dibutyltin diacetate as starting materials were thoroughly investigated, revealing that the sample calcined at 500ºC for 2 h showed the best electrochemical performance amongst sample a, b and c. It was revealed that the relatively higher crystallinity, the higher content of Sn element, the presence of a proper amount of carbon spheres, the special three-dimensional structure, the smallest value of R_{ct} and the larger value of D_{Li+} were the main reasons endowing sample b with a superior electrochemical performance when compared to sample a and c.

4. CONCLUSIONS

For the first time, flower-shaped tin dioxide (SnO_2) micron-sized particles were prepared via a very simple method of an air calcination process using dibutyltin diacetate as the starting material, in which carbon spheres and flaky SnO_2 particles were simultaneously produced. The influence of the calcination temperature on the properties of the calcination products was systematically examined in the first part of this work, revealing that SnO_2 with a relatively higher crystallinity was the main component of all prepared samples based on the XRD pattern and XPS analysis. SEM images

indicated that spherical micron-sized particles, flower-shaped particles and layered square rock-shaped particles were, respectively, observed in sample a, b and c. Most importantly, the DC value at 100 mA g^{-1} of sample b after 20 cycles was maintained as high as 325 mAh g^{-1}, indicating that sample b was a promising anode material of LIBs. The higher crystallinity, the larger content of Sn element, the proper amount of carbon spheres, the special three-dimensional structure, the smallest value of R_{ct} and the larger value of D_{Li+} were thought to be the main reasons providing sample b with a superior electrochemical performance when compared to other samples. Showing a very simple calcination method to prepare flower-shaped SnO_2 micron-sized particles, and preparing a novel LIBs anode material as well, was the main dedication of this work, which will open up a novel SnO_2-related research field since all the works shown in this work have never been reported previously.

ACKNOWLEDGEMENTS
This work was funded by Science and Technology Project of Hebei Education Department (No. ZD2020327).

References

1. J. Li, K. Lim, H. Yang, Z. Ren, S. Raghavan, P.-Y. Chen, T. Buonassisi and X. Wang, *Matter,* 3 (2020) 393.
2. M.-S. Kim, B.-H. Lee, J.-H. Park, H. S. Lee, W. H. Antink, E. Jung, J. Kim, T. Y. Yoo, C. W. Lee, C.-Y. Ahn, S. M. Kang, J. Bok, W. Ko, X. Wang, S.-P. Cho, S.-H. Yu, T. Hyeon and Y.-E. Sung, *J. Am. Chem. Soc.,* 142 (2020) 13406.
3. F. Wang, Y. Deng and C. Yuan, *Procedia Manufacturing,* 49 (2020) 24.
4. B. L. D. Rinkel, D. S. Hall, I. Temprano and C. P. Grey, *J. Am. Chem. Soc.,* 142 (2020) 15058.
5. K. Wang, J. Wan, Y. Xiang, J. Zhu, Q. Leng, M. Wang, L. Xu and Y. Yang, *J. Power Sources,* 460 (2020) 228062.
6. Y. Li, Q. Li and Z. Tan, *J. Power Sources,* 443 (2019) 227262.
7. H.-P. Lin, K.-T. Chen, C.-B. Chang and H.-Y. Tuan, *J. Power Sources,* 465 (2020) 228262.
8. C. Sun, Y.-J. Wang, H. Gu, H. Fan, G. Yang, A. Ignaszak , X. Tang, D. Liu and J. Zhang, *Nano Energy,* 77 (2020) 105092.
9. C. Gao, Z. Jiang, P. Wang, L. R. Jensen, Y. Zhang and Y. Yue, *Nano Energy,* 74 (2020) 104868.
10. L. Wang, X. Zhu, K. Tu, D. Liu, H. Tang, J. Li, X. Li, Z.-Z. Xie and D. Qu, *Electrochim. Acta,* 354 (2020) 136726.
11. Z. Wang, X. Zhang, X. Liu, Y. Wang, Y. Zhang, Y. Li, W. Zhao, C. Qin, A. Mukanova and Z. Bakenov, *J. Power Sources,* 449 (2020) 227550.
12. G. Zhang, Y. Shi, H. Wang, L. Jiang, X. Yu, S. Jing, S. Xing and P. Tsiakaras, *J. Power Sources,*416 (2019) 118.
13. X. Liu, C. Shen, J. Lu, G. Liu, Y. Jiang, Y. Gao, W. Li,B. Zhao and J. Zhang, *Electrochim. Acta,* 361 (2020) 137074.
14. S. Liang, X. Pei, W. Jiang, Z. Xu, W. Wang, K. Teng, C. Wang, H. Fu and X. Zhang, *Electrochim. Acta,* 322 (2019) 134696.
15. Y. Feng, K. Wu, J. Ke, H. Dong, X. Huang, C. Bai, D. Xiong and M. He, *J. Power Sources,* 467 (2020) 228357.
16. X. Zhou, L. Yu and X. W. Lou, *Nanoscale,* 8 (2016) 8384.
17. R. Tian, Y. Zhang, Z. Chen, H. Duan, B.Xu, Y. Guo, H. Kang, H. Li and H. Liu, *Sci. Rep.,* 6 (2016) 19195.
18. B. Jiang, Y. He, B. Li, S. Zhao, S. Wang, Y.-B. He and Z. Lin, *Angew. Chem., Int. Ed.,* 56 (2017) 1.
19. R. Hu, Y. Ouyang, T. Liang, H. Wang, J. Liu, J. Chen, C. Yang, L. Yang and M. Zhu, *Adv. Mater.,*

(2017) 1605006.
20. L. Paul Wang, Y. Leconte, Z. Feng, C. Wei, Y. Zhao, Q.Ma, W. Xu, S. Bourrioux, P. Azais, M. Srinivasan and Z. J. Xu, *Adv. Mater.,* (2016) 1603286.
21. D. Liu, Z. Kong, X. Liu, A. Fu, Y. Wang, Y.-G. Guo, P. Guo, H. Li and X. S. Zhao, *ACS Appl. Mater. Interfaces,* 10 (2018) 2515.
22. Y. Yang, X. Zhao, H.-E. Wang, M. Li, C. Hao, M. Ji, S. Ren and G. Cao, *J. Mater. Chem. A,* 6 (2018) 3479.
23. S. Gao, N. Wang, S. Li, D. Li, Z. Cui, G. Yue, J. Liu, X. Zhao, L. Jiang and Y. Zhao, *Angew. Chem., Int. Ed.,* 59 (2020) 2465.
24. D. Wei, F. Xu, J. Xu, J. Fang, S. W. Koh, K. Li and Z. Sun, *Ceram. Int.,* 46 (2020) 1396.
25. Z. Hu, X. Xu, X. Wang, K. Yu and C. Liang, *J. Alloys Compd.*, 835 (2020) 155446.
26. J. Liang, C. Yuan, H. Li, K. Fan, Z. Wei, H. Sun and J. Ma, *Nano-Micro Lett.,* 10 (2018) 21.
27. X. Sun, Y. Li, *Angew. Chem., Int. Ed.,* 43 (2004) 597.
28. C. Zhang, K. B. Hatzell, M. Boota, B. Dyatkin, M. Beidaghi, D. Long, W. Qiao, E. C. Kumbur and Y. Gogotsi, *Carbon,* 77 (2014) 155.
29. 29.Y. Fan, P. F. Liu, Z. Y. Huang, T. W. Jiang, K. L. Yao and R. Han, *J. Power Sources,* 280 (2015) 30.
30. S. Zhang, L. Zhang, L. Qian, J. Yang, Z. Ao, and W. Liu, *ACS Sustainable Chem. Eng.,*7(2019)7486.
31. J. Wang, C. Yang, J. Wang, L. Han and M. Wei, *Electrochim. Acta*, 295 (2019) 246.
32. K. Ding, Y. zhao, L. Liu, Y. Li, L. Liu, L. Wang, X. He and Z. H. Guo, *Electrochim. Acta*, 176 (2015) 240.
33. R. Gao, J. Tang, X. Yu, S. Tang, K. Ozawa, T. Sasaki and L.-C. Qin, *Nano Energy,* 70 (2020) 104444.
34. X. Miao, X. Ge, P. Wang, D. Zhao and L. Yin, *Electrochim. Acta,* 356 (2020) 136769.
35. K. Ding, L. Zhou, R. Qu, D. Zhang, J. Chen, X. He, L. Wang, H. Wang and H. Dou， *Mater. Chem. Phys.,* 251 (2020) 123202.
36. J. Cao, C. Qin and Y. Wang, *J. Alloys Compd.,* 728 (2017) 1101.
37. Y. Fan, P.-F. Liu, Z.-Y. Huang, T.-W. Jiang, K.-L. Yao and R. Han, *J. Power Sources,* 280 (2015) 30.
38. K. Ding, Y. Zhao, M. Zhao, Y. Li, J. Zhao, Y. Chen and Q. Wang, *Int. J. Electrochem. Sci.,* 10 (2015) 7917.
39. K. Ding, J. Han, X. Gao, L. Wang, L. Zhou, R. Qu and X. He, *Int. J. Hydrogen Energy,* 45 (2020) 1930.
40. J. Liang, C. Yuan, H. Li, K. Fan, Z. Wei, H. Sun and J. Ma , *Nano-Micro Lett.,* 10 (2018) 21.
41. A.M. Puziy, O.I. Poddubnaya, R.P. Socha, J. Gurgul and M. Wisniewski, *Carbon,* 46 (2008) 2113.
42. R. Tian, Y. Zhang, Z. Chen, H. Duan, B. Xu, Y. Guo, H. Kang, H. Li and H. Liu, *Sci. Rep.,* 6 (2016) 19195.
43. D. Wei, F. Xu, J. Xu, J. Fang, S. W. Koh, K. Li and Z. Sun, *Ceram. Int.,* 46 (2020) 1396.
44. K. Ding, H. Gu, C. Zheng, L. Liu, L. Liu, X. Yan and Z. Guo, *Electrochim. Acta,* 146 (2014) 585.
45. K. Ding, B. Wei, Y. Zhang, C. Li, X. Shi and J. Pan, *Int. J. Electrochem. Sci.,* 12 (2017) 8381.
46. T.-F. Yi, H. Liu, Y.-R. Zhu, L.-J. Jiang, Y. Xie and R.-S. Zhu, *J. Power Sources,* 215 (2012) 258.
47. B. Jin, E.M. Jin, K.-H. Park and H.-B. Gu, *Electrochem. Commun.,* 10 (2008) 1537.
48. W. Wang , P. Zhang , S. Li , C. Zhou , S. Guo , J. Liu , J. Zhou , X. Jian , Y. Yang , Y. Lei , K. Li , J. Wu and L. Chen, *J. Power Sources,* 475 (2020) 228683.